

1 **Interference of extracellular soluble algal organic matter on flocculation–sedimentation harvesting**
2 **of *Chlorella* sp.**

3

4 **Abstract**

5 Extracellular soluble algal organic matter (AOM) significantly influences microalgae flocculation. This
6 study investigated the effects of various AOM fractions on *Chlorella* sp. flocculation using ferric
7 chloride (FeCl₃), sodium hydroxide (NaOH), and chitosan. All flocculants achieved high separation
8 efficiency (87–99%), but higher dosages were required in the presence of AOM. High molecular
9 weight (>50 kDa) AOM fraction was identified as the primary inhibitor of flocculation across different
10 pH levels, whereas low/medium molecular weight (<3 and <50 kDa) AOM had minimal impact.
11 Compositional analysis revealed that the inhibitory AOM fraction is a glycoprotein rich in
12 carbohydrates, including neutral, amino, and acidic sugars. The significance of this study is in
13 identifying carboxyl groups (–COOH) from acidic monomers in >50 kDa AOM that inhibit flocculation.
14 Understanding AOM composition and the interaction dynamics between AOM, cells, and flocculants
15 is crucial for enhancing the techno-economics and sustainability of flocculation-based microalgae
16 harvesting.

17

18 **Keywords:** Microalgae, Biomass, Dewatering, Ultrafiltration, Heteropolysaccharides

19 **1 Introduction**

20 Microalgae have garnered significant attention as an industrial biomass feedstock due to their
21 potential in producing proteins, carbohydrates, lipids, pigments, and specialty chemicals (Shitanaka
22 et al., 2024). The production of microalgal biomass involves several key steps: species-strain
23 selection, cultivation, harvesting, and downstream processing into desired products (Qin et al.,
24 2023). Despite advancements in these areas, efficient and cost-effective harvesting remains a major
25 hurdle for commercializing microalgae-based products (McGrath et al., 2024; Qin et al., 2023).

26 Various solid-liquid separation methods, such as centrifugation, screening, filtration, gravity
27 sedimentation, flocculation, flotation, etc., have been explored for microalgae harvesting (Liu et al.,
28 2023). Among these, flocculation-based methods as a primary dewatering step are particularly
29 promising due to their energy efficiency and scalability (Liu et al., 2023; McGrath et al., 2024).

30 However, the effectiveness of flocculation is influenced by several factors, including species type, cell
31 morphology, medium composition, ionic strength, pH, etc. (Henderson et al., 2008; Lama et al.,
32 2016). Moreover, a key determinant of the economic viability of flocculation is the type, cost, and
33 dosage of flocculants used (Liu et al., 2023). Thus, a fundamental understanding of interaction
34 dynamics between microalgal cells, flocculants, and medium components is crucial.

35 One of the critical medium components affecting the microalgal flocculation process is the
36 extracellular algal organic matter (AOM) (Cheng et al., 2024; Zang et al., 2020; Zhang et al., 2024).
37 AOM is a complex mixture of organic compounds released by algal cells, predominantly composed of
38 polysaccharides (up to 88%) and proteins (up to 67%) with a net negative charge (Naveed et al.,
39 2019; Zhou et al., 2024). Previous studies have demonstrated that AOM can inhibit flocculation by
40 competing with cells for positively charged flocculants (Cheng et al., 2022; Pivokonsky et al., 2012;
41 Zang et al., 2020). Some studies have shown that the extensive network of AOM may induce the
42 bridging of cells in the presence of positively charged flocculants (Cheng et al., 2024; Vu et al., 2021;
43 Zhang et al., 2024). Nevertheless, its specific role in flocculation-based microalgal biomass harvesting

44 remains insufficiently explored. Hence, detailed AOM compositional analysis could provide further
45 insights into the interaction mechanism of AOM, cells, and flocculants (Rao et al., 2020; Yang et al.,
46 2020). Understanding the quantity and composition of AOM and its influence on different
47 flocculation methods will offer valuable insights for selecting effective flocculants. Moreover,
48 identifying the active functional groups in AOM can render new avenues for utilizing AOM as a
49 flocculant aid or *in situ* flocculating agent, with direct implications for enhancing the economic
50 viability and environmental sustainability of microalgae biomass production.

51 This study focuses on understanding the interference of AOM in the flocculation of *Chlorella* sp.,
52 producing a substantial quantity of AOM during the early stationary phase. Unlike previous studies
53 that broadly address the impact of AOM, this study breaks down AOM into specific molecular weight
54 fractions via sequential ultrafiltration and investigates their roles in flocculation induced by ferric
55 chloride (FeCl₃), sodium hydroxide (NaOH), and chitosan, each having a unique flocculation
56 mechanism. Employing advanced non-destructive analytical techniques, such as Fourier transform
57 infrared spectroscopy (FTIR) and solid-state ¹³C-NMR spectroscopy, facilitates a comprehensive
58 analysis of AOM composition, pinpointing specific functional groups responsible for flocculation
59 interference. This novel approach will provide valuable insights into the interactions between AOM
60 and flocculants under various pH conditions, paving the way for improved microalgae harvesting
61 strategies. The results of this study not only advance the understanding of AOM's role in flocculation
62 but also propose tailored approaches to enhance flocculation efficiency in microalgal biomass
63 recovery.

64 **2 Materials and methods**

65 **2.1 Cultivation of *Chlorella* sp.**

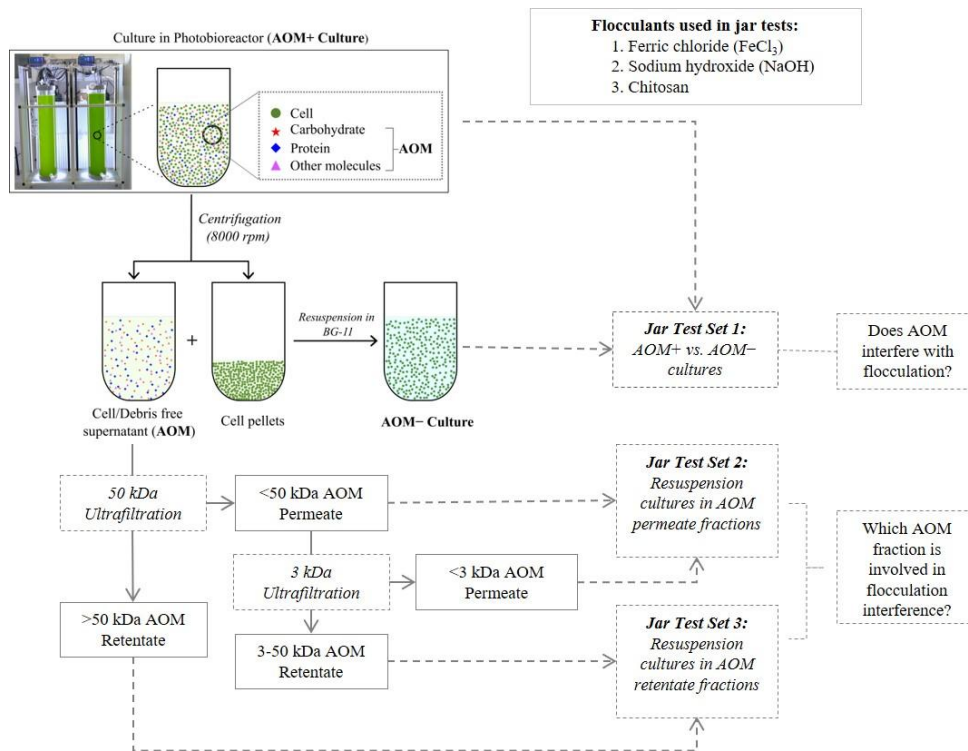
66 Freshwater green microalga *Chlorella* sp. (kindly provided by Ecotoxicology and Environmental
67 Services Laboratory of the National Center of Applied Electromagnetism, Universidad de Oriente,
68 Cuba) was cultivated in nitrate-modified (100 mg·L⁻¹ NO₃⁻) BG-11 medium prepared with sterilized

69 deionized water (Wu et al., 2012). The cultivation was done in two identical bubble column
70 photobioreactors (25 L, length × diameter: 100 cm × 20 cm) at room temperature (20±2 °C). The
71 culture was mixed using 0.2 µm filtered air (2 L min⁻¹), with the pH maintained at 8.50 by dosing pure
72 pressurized CO₂ via pH-controller system (DENNERLE, pH-Controller Evolution DeLuxe). Each
73 photobioreactor was illuminated on two opposite sides with LED lights (7000K- daylight, 4000K-warm
74 white, and RGB colored 1200 mm GoldLine LED, HVP Aqua) in a 16:8 h light: dark cycle, providing a
75 photon flux density of approximately 150 µmol photons m⁻² s⁻¹ at the reactor surface. Culture growth
76 was monitored by measuring optical density at 750 nm (OD₇₅₀) using a UV–visible spectrophotometer
77 (Ultraspec–7000). The OD₇₅₀-based growth curve was fitted with a growth sigmoidal function
78 (Sigmoidal Logistics Function, Origin 2020) (Ajala & Alexander, 2020). Additionally, OD₇₅₀ was
79 calibrated (linear fit) against microalgal dry weight (DW) biomass concentration (g L⁻¹), which was
80 determined gravimetrically. This involved filtering a known volume of culture on pre-weighed glass
81 microfiber filters (Whatman GF6, 47 mm diameter) and drying overnight at 105°C. Overall, 50 L of
82 culture (from 2×25 L photobioreactors) was consumed during the experimental procedure.

83 **2.2 Isolation of extracellular soluble algal organic matter (AOM)**

84 The culture at any growth phase from the photobioreactor is referred to hereafter as a culture with
85 extracellular soluble algal organic matter (AOM), designated as AOM+ culture. A culture suspension
86 without AOM, designated as AOM– culture, was prepared by resuspending centrifuged cell pellets in
87 fresh nitrate-modified BG-11 medium (Vandamme et al., 2016). Cell/debris-free culture supernatant
88 obtained after centrifugation of AOM+ culture is referred to as extracellular soluble algal organic
89 matter (AOM) (Figure 1) (Rao et al., 2020). Centrifugation was performed at 8000 rpm (~5000 ×g) (FJ
90 130 EPR, Milky Day, Czech Republic) and repeated 2-3 times until the supernatant was cell/debris-
91 free. Approximately 20 L of AOM was isolated from the early stationary phase (day 15) culture for
92 fractionation (ultrafiltration) to obtain different molecular weight fractions for the flocculation
93 experiments. AOM was collected during the early stationary phase, when cell growth has slowed, but

94 cell lysis and release of intracellular or cell wall components were minimal. Thus, AOM isolated
 95 mainly comprises cell-secreted or surface-dissociated dissolved/soluble extracellular organic matter
 96 (Rao et al., 2020; Villacorte et al., 2015; Vu et al., 2021).



97
 98 **Figure 1:** Experimental overview for AOM isolation/fractionation and flocculation jar tests for various
 99 culture suspensions: AOM+, AOM-, and AOM fractions resuspension cultures.

100 **2.3 Ultrafiltration of algal organic matter (AOM)**

101 Ultrafiltration of AOM (20 L, day 15) was conducted using a tangential flow filtration system (ÄKTA
 102 flux 6, Cytiva). The first ultrafiltration step employed a hollow-fiber filter cartridge with a nominal
 103 molecular weight cut-off (NMWCO) of 50 kDa and a membrane area of 0.14 m² (UFP-50-C-4X2MA,
 104 Cytiva). This process operated at constant transmembrane pressure (TMP) of 60 kPa in retentate
 105 recycle mode, concentrating the feed AOM solution 36-fold. The <50 kDa AOM permeate fraction
 106 (~18 L) from this step was divided, with 10 L used for further ultrafiltration with a 3 kDa filter and 8 L
 107 stored at 4°C for flocculation resuspension jar tests (set 2). The second ultrafiltration of <50 kDa AOM
 108 permeate fraction was performed with a 3 kDa NMWCO filter (UFP-3-C-4X2MA, membrane area of
 109 0.14 m², Cytiva) at 70 kPa TMP, concentrating the feed solution 21-fold. The <3 kDa AOM permeate

110 fraction (~8 L) was collected and stored at 4°C until further use in the flocculation resuspension jar
111 tests (set 2). Concentrated AOM retentate fractions (>50 kDa and 3–50 kDa) from each ultrafiltration
112 were dialyzed with distilled water until the water permeate conductivity (inoLab Cond 7110)
113 decreased from 650 $\mu\text{S cm}^{-1}$ to less than 20 $\mu\text{S cm}^{-1}$. Approximately half of the concentrated liquid
114 AOM (>50 kDa fraction) was lyophilized for 48 h at –40°C under 12 Pa vacuum pressure (CHRIST,
115 ALPHA 1–2 LDPlus). This process yielded 1.36 g L⁻¹ of lyophilized >50 kDa AOM. Both lyophilized and
116 remaining liquid AOM fractions were stored at –20°C until further use in analysis and jar tests (set 3)
117 with AOM retentate fraction.

118 2.4 Total organic carbon, total nitrogen, and elemental composition

119 The total organic carbon (TOC), measured as non-purgeable organic carbon, and total nitrogen (TN)
120 in AOM were assessed daily during the culture growth using a TOC analyzer (TOC–L_{CPH}, Shimadzu
121 Benelux). The concentrations of readily available elements (Al, B, Ca, Fe, K, Mg, Mn, Na) were
122 determined with an inductively coupled plasma optical emission spectrometer (ICP–OES) (Perkin
123 Elmer Optima 8300). Anions (NO_3^- , NO_2^- , Cl^- , PO_4^{3-} , SO_4^{2-}) were measured by ion chromatography
124 (Thermo Scientific Dionex ICS–6000) using Dionex IonPac AS14A column (4x250 mm).

125 2.5 Flocculation experiments

126 2.5.1 Flocculant stock solutions

127 Fresh stock solutions of 10 g·L⁻¹ ferric chloride (Merck) and 0.5 M sodium hydroxide (Sigma–Aldrich)
128 were prepared in Milli–Q water. Chitosan (molecular weight: 100–300 kDa, Acros Organics) stock of 5
129 g·L⁻¹ was prepared in 0.04 M of HCl (VWR Chemicals) by rapidly mixing (500 rpm) the solution
130 mixture for 1.5 h.

131 2.5.2 Jar test procedure

132 All the jar tests were performed with microalga culture suspension maintained at an equivalent dry
133 biomass concentration of 0.60±0.05 g·L⁻¹ and an initial pH of 8.50±0.15 at room temperature

134 (20±2°C). Culture suspension (100 mL) was distributed in a series of 10–15 transparent plastic jars
 135 (VWR, 216–1830) placed over a multi-position magnetic stirrer (IKA RO 15). Each flocculant stock
 136 solution was added to the culture suspensions to achieve a final concentration of 0–1000 mg·L⁻¹. For
 137 NaOH flocculation jar test, 10 mM of magnesium chloride hexahydrate (VWR Chemicals BDH) was
 138 added to a culture suspension before sodium hydroxide dosing (Fan et al., 2017; Vandamme et al.,
 139 2016; Wu et al., 2012). During flocculant addition, culture suspensions were vigorously mixed at 350
 140 rpm for 10 minutes, followed by gentle mixing at 250 rpm for 20 minutes. The pH of each jar
 141 (measured with a Knick pH–Meter 764 Multi-Calimatic) was noted at the end of the rapid mixing
 142 phase. After mixing, suspensions were allowed to settle for 30 min, and 3.3 mL samples were
 143 collected from approximately 1.5 cm below the suspension surface for optical density (OD₇₅₀)
 144 measurement. The separation efficiency (SE %) for each treatment was estimated using Eq. (1):

$$145 \text{ Separation Efficiency (SE \%)} = \frac{OD_i - OD_f}{OD_i} \times 100 \quad (1)$$

146 Where OD_i and OD_f are OD_{750} measurements before flocculant addition and after settling,
 147 respectively (Lama et al., 2016; Vandamme et al., 2012). Based on the resulting series of SE (%)
 148 achieved against applied dosage (mg g⁻¹ of dry biomass), dose-response curve fitting was performed
 149 by using a sigmoidal regression model (Boltzmann function, Origin 2020). The model is defined in Eq.
 150 (2) as follows (Lama et al., 2016; Zhang et al., 2012):

$$151 y = A_2 + \frac{A_1 - A_2}{1 + e^{\left(\frac{x - x_0}{dx}\right)}} \quad (2)$$

152 where y is response value (SE %) depending on flocculant dosage (x). Flocculant dosage at the
 153 inflection point (x_0)—a midpoint of the sigmoidal curve—represents the minimum dosage required to
 154 induce flocculation. A slope factor (dx) at the inflection point determines a curve's steepness and,
 155 thus, the sensitivity of the SE to the flocculant dosage. For high dx , increase in SE is slow, while for
 156 low dx , increase is rapid. A_1 and A_2 are the response values (SE %) corresponding to the asymptotes

157 on the minimum and maximum boundaries of the curve. Additionally, the optimum flocculant
158 dosage— minimum dosage corresponding to the maximum SE (A_2)— was used as a reference dosage
159 in subsequent jar tests.

160 **2.5.3 Jar test on cultures with (AOM+) and without (AOM-) algal organic matter (Jar test set 1)**

161 Effect of AOM in the flocculation process was assessed by jar tests on AOM+ and AOM- culture
162 suspensions (day 18 culture, $DW=0.63 \text{ g}\cdot\text{L}^{-1}$, pH 8.50). AOM- culture was prepared by resuspension
163 of centrifuged AOM+ culture cells pellet in fresh BG-11 medium. A desired biomass concentration in
164 resuspension was maintained by adjusting OD_{750} with reference from the OD_{750} vs. DW linear fit (DW
165 $= 0.2776\pm 0.0044\times OD_{750} - 0.0229\pm 0.0076$, $R^2 = 0.98$). Jar tests were carried out as detailed in the jar
166 test procedure.

167 **2.5.4 Jar test on AOM permeate (<50 kDa and <3 kDa) resuspension cultures (Jar test set 2)**

168 Flocculation jar tests (as detailed in the jar test procedure) were performed on AOM+, AOM-, <50
169 kDa, and <3 kDa resuspension cultures to evaluate the effect of low/medium molecular weight AOM
170 fractions. AOM and its fractions used in this test were processed in advance using the early
171 stationary phase (day 15) culture, as detailed in the AOM isolation and ultrafiltration section.
172 Centrifuged cells (day 19) were resuspended in AOM (day 15), fresh BG-11 medium, <50 kDa and <3
173 kDa AOM permeate fractions to make AOM+, AOM-, <50 kDa, and <3 kDa AOM culture suspensions
174 ($0.60 \text{ g}\cdot\text{L}^{-1}$, pH 8.50). The flocculation jar tests were conducted following the procedure detailed in
175 the jar test protocol.

176 **2.5.5 Jar test on AOM retentate (>50 kDa) resuspension cultures (Jar test set 3)**

177 The effect of high molecular weight (>50 kDa) AOM fraction in the flocculation was determined by
178 performing resuspension jar tests with >50 kDa AOM retentate fraction (liquid, 36-fold concentrated,
179 lyophilized yield of 1.36 g L^{-1}) obtained in the ultrafiltration section. A slight modification was made
180 to the jar test procedure before the addition of flocculant stocks. Liquid AOM (concentrated >50 kDa

181 fraction) was added in increasing concentrations (equivalent TOC concentrations of 0–35 mg L⁻¹) to
182 the AOM– culture suspension (0.60 g·L⁻¹, pH 8.50). During the addition of the AOM fraction, the
183 culture suspension was homogeneously mixed at 400 rpm for 5 minutes. Flocculant stocks were
184 added to attain a final concentration of 135.0, 235.0, and 65.0 mg g⁻¹ dry biomass of FeCl₃, NaOH,
185 and chitosan, respectively. These flocculant dosages correspond to optimum dosages, which
186 achieved maximum separation efficiencies (≥98 %) in AOM– culture jar test set 1. Following the
187 addition of flocculants, all procedures were carried out as outlined in the jar test procedure.

188 2.6 Compositional analysis of AOM retentate (>50 kDa) fraction

189 2.6.1 Fourier–transform infrared (FTIR) spectroscopy

190 Fourier–transform infrared (FTIR) spectroscopy of lyophilized >50 kDa AOM (day 15 AOM obtained as
191 detailed in the ultrafiltration section) was performed with a Vertex 70 spectrometer equipped with a
192 deuterated triglycine sulfate (DTGS) detector (Bruker, Karlsruhe, Germany) in attenuated total
193 reflection (ATR) mode using a diamond crystal (PIKE, Fitchburg, USA). Thirty-two scans per sample
194 were obtained in the 4000–600 cm⁻¹ spectral region at a resolution of 4 cm⁻¹. Baseline correction and
195 normalization were performed on the largest peak, which varied for each sample. Band assignments
196 were made following numerous reference studies (Capek et al., 2008; Cybulska et al., 2016; Liu et al.,
197 2021; Pinel et al., 2020; Villacorte et al., 2015).

198 2.6.2 Solid–state ¹³C–Nuclear magnetic resonance (NMR) spectroscopy

199 Solid-state ¹³C–CP/MAS (Cross Polarization/Magic Angle Spinning) NMR experiments were performed
200 on a Varian VNMRS 400 MHz spectrometer (9.4 T, Agilent) using a T3HX 3.2 mm VT probe.
201 Lyophilized >50 kDa AOM (80 mg, day 15 AOM obtained as detailed in the ultrafiltration section) was
202 introduced into airtight ceramic zirconia rotors of 3.2 mm in diameter (22 µL rotors). Spectra were
203 recorded with a MAS spinning frequency of 15 kHz at 25 °C. The aromatic signal of
204 hexamethylbenzene was used to determine the Hartmann–Hahn condition for cross-polarization and
205 to calibrate the carbon chemical shift scale (132.1 ppm). Acquisition parameters were as follows: a

206 spectral width of 50 kHz, a 90° pulse length of 2.5 μs, a contact time for cross-polarization of 1.0 ms,
207 an acquisition time of 20.0 ms, a recycle delay time of 2.5 s, and approximately 30,000 scans. High-
208 power proton dipolar decoupling during the acquisition time was set to 85 kHz (Arnold et al., 2015).
209 Spectra were processed using Delta software (version 6.3.0, Jeol).

210 **2.6.3 Total carbohydrate, total protein, and monosaccharide composition analysis**

211 AOM stock solution was prepared by dissolving 5 mg of lyophilized >50 kDa AOM (day 15 AOM
212 obtained as detailed in the ultrafiltration section) in 5 mL of Milli-Q water under continuous stirring
213 overnight at 4°C. For acid hydrolysis, 100 μL AOM stock solution was transferred to screw-cap Pyrex
214 tubes and dried under a nitrogen stream. Then, 1 mL of 3 M Methanolic HCl (Merck) was added to
215 the dried tube and incubated at 95°C for 3 h, followed by cooling in an ice bath for 5 minutes and
216 subsequent drying under a nitrogen stream at 25°C. The second hydrolysis step involved adding 1 mL
217 of 2 M trifluoroacetic acid (Merck), followed by heating at 121°C for 1 h and drying under a nitrogen
218 stream (Nagel et al., 2014). The dried hydrolysate was resuspended with 2 mL of Milli-Q water. Any
219 further dilution required was done with Milli-Q and filtered (Nylon 0.22 μm) before analysis. Total
220 carbohydrate content was determined with 500 μL of hydrolysate using the 3-methyl-2-
221 benzothiazolinone hydrazone (MBTH) method, with D-glucose (Sigma, BioXtra, ≥99.5 %) as standard
222 (Van Wychen & Laurens, 2016). Total protein was quantified with 500 μL of aliquots using a Pierce
223 BCA Protein Assay Kit (Thermo Scientific, Product: 23227).

224 Monosaccharide composition was analyzed using a high-performance anion-exchange
225 chromatography system with pulsed amperometric detection (HPAEC-PAD) (Thermo Scientific
226 Dionex ICS-6000). The system included a CarboPac PA20 guard column (3 × 50 mm) and a CarboPac
227 PA20 analytical column (3 × 150 mm) maintained at 20°C. The detector was equipped with a non-
228 disposable gold working electrode and palladium hydrogen (PdH) reference electrode, applying the
229 standard carbohydrate quadrupole-potential waveform (Chromeleon software version 7.3.1). The
230 autosampler was set for a full loop sample injection volume of 25 μL at a flow rate of 0.4 mL/min.

231 The eluent consists of four different channels, namely: A: Milli-Q water, B: 10 mM sodium hydroxide
232 (NaOH) + 10 mM sodium acetate (NaAce), C: 100 mM NaOH + 100 mM NaAce, and D: 100 mM NaOH.
233 The following gradient was applied: 0–25 min 94 % A; 5 % B, 1% D; 25–27 min 45 % A; 5 % B, 50% D;
234 27–46 min 100 % C; 46–50 min 100 % D; 50–60 min 94 % A; 5 % B, 1% D. **Detection and quantification**
235 **of analytes** were done by using calibration standards (0.1, 0.2, 0.5, 0.8, 1.0, 2.0, 3.0, 4.0 $\mu\text{g}\cdot\text{mL}^{-1}$) of
236 12 mixed monosaccharides: **neutral (fucose, rhamnose, arabinose, galactose, glucose, xylose,**
237 **mannose, and ribose); amino (galactosamine and glucosamine); and acidic (galacturonic acid and**
238 **glucuronic acid).** The total carbohydrate, protein, and monomer **composition were** expressed as
239 weight percentage (wt %) of the lyophilized >50 kDa AOM sample.

240 **2.7 Statistical Analysis**

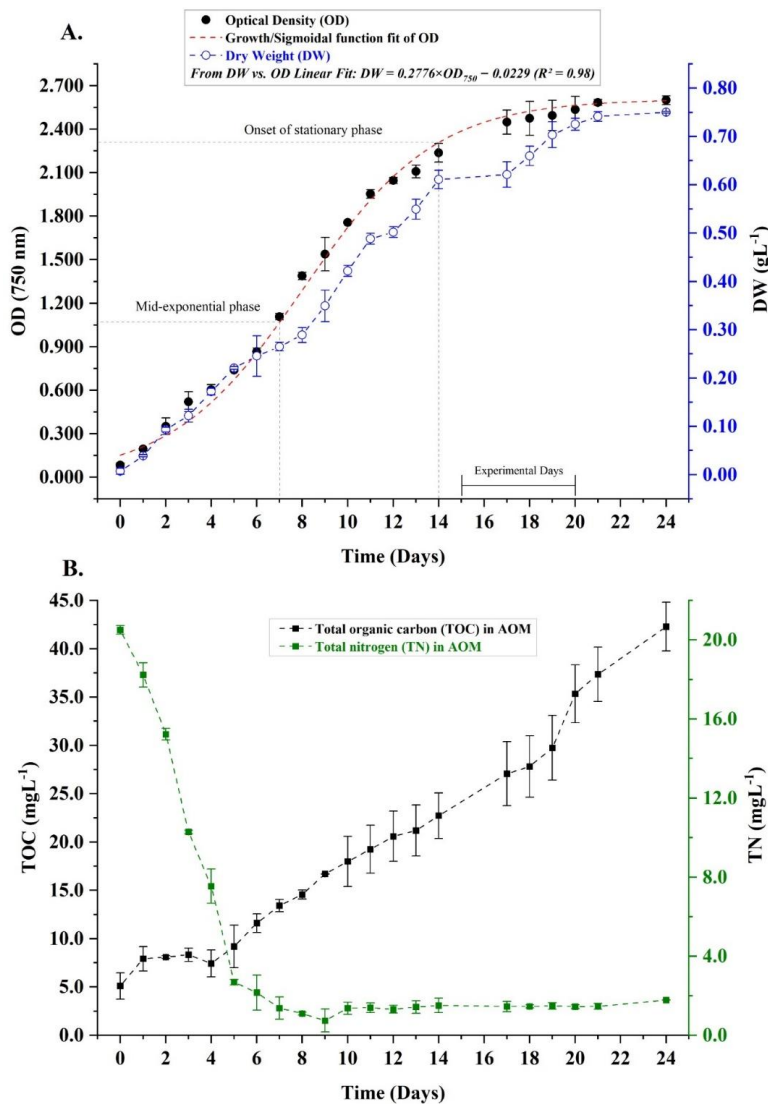
241 In addition to sigmoidal regression for all dose-response results, one-way ANOVA followed by Tukey's
242 mean comparison test (Origin 2020) was performed to evaluate the significance differences ($p < 0.05$)
243 among the results obtained on separation efficiencies, dosages, TOC concentrations of AOM+,
244 AOM-, and resuspension cultures. The analytical results represent the average of triplicate
245 measurements.

246 **3 Result and discussion**

247 **3.1 Culture growth characteristics**

248 **Culture** growth was monitored daily by **measuring** optical density (OD_{750}) and dry weight (DW)
249 (Figure 2A). **Biomass DW** followed a similar trend to OD_{750} (Linear fit: $\text{DW} = 0.2776 \pm 0.0044 \times \text{OD}_{750} -$
250 0.0229 ± 0.0076 , $R^2 = 0.98$) over the growth period, attaining 0.6–0.7 $\text{g}\cdot\text{L}^{-1}$ during jar test experimental
251 days (day 15–20). A midpoint of the OD_{750} -based growth curve **indicates a mid-exponential** phase
252 **around day 7. The stationary phase began on day 14 and lasted until day 30, with no observed**
253 **decline phase. On the inoculation day, medium nitrate (NO_3^-) and phosphate (PO_4^{3-}) levels were**
254 **91.4 \pm 1.3 $\text{mg}\cdot\text{L}^{-1}$ and 20.0 \pm 0.3 $\text{mg}\cdot\text{L}^{-1}$, respectively, and they depleted to <2.5 $\text{mg}\cdot\text{L}^{-1}$ and 8.6 \pm 1.5**
255 **$\text{mg}\cdot\text{L}^{-1}$ on day 7, corresponding to mid-exponential growth phase in OD_{750} based growth curve.**

256 Additionally, total organic carbon (TOC) in the extracellular soluble algal organic matter (AOM)
 257 increased throughout the growth period—from $5.1 \pm 1.4 \text{ mg}\cdot\text{L}^{-1}$ on inoculation day to $27.8 \pm 3.2 \text{ mg}\cdot\text{L}^{-1}$
 258 on day 18—indicating the accumulation of organic matter in the culture (Vu et al., 2021; Zhang et al.,
 259 2012). However, total nitrogen (TN) in the AOM decreased over time, from $20.5 \pm 0.2 \text{ mg}\cdot\text{L}^{-1}$ on
 260 inoculation day to $<2.0 \text{ mg}\cdot\text{L}^{-1}$ on day 7 onwards (Figure 2B). TN measured on inoculation day can be
 261 attributed to the culture medium nitrate (N-NO_3^-). Rapid decrease in TN over the growth period is
 262 consistent with medium nitrate depletion due to assimilation by growing cells (Ajala & Alexander,
 263 2020). Overall, culture growth in both photobioreactors was consistent and replicable in terms of
 264 OD_{750} , DW, NO_3^- , PO_4^{3-} , TOC, and TN measurements.



265

266 **Figure 2: A:** Growth curve of *Chlorella* sp.; OD values are fitted (Red dashed curve) with a sigmoidal
267 function to observe growth phases. The equation of DW and OD₇₅₀ is derived from the linear fit of OD
268 values and corresponding dry weights measured. **B: Measurement of TOC and TN in culture AOM**
269 **throughout growth.**

270

271 **3.2 Interference of total algal organic matter (AOM) in flocculation (Jar test set 1)**

272 The effect of total/whole AOM in the flocculation was evaluated by jar test on early stationary phase

273 (day 18) AOM+ and AOM- cultures using three flocculants: FeCl₃, NaOH, and chitosan. A sigmoidal

274 dose-response model of the separation efficiency (SE %) against the flocculant dosage was a good fit

275 with the experimental data ($R^2 > 0.99$). The inflection point dosage (x_0) was used to compare dose

276 responses of AOM+ and AOM- cultures (Figure 3). Additionally, the optimum flocculant dosage

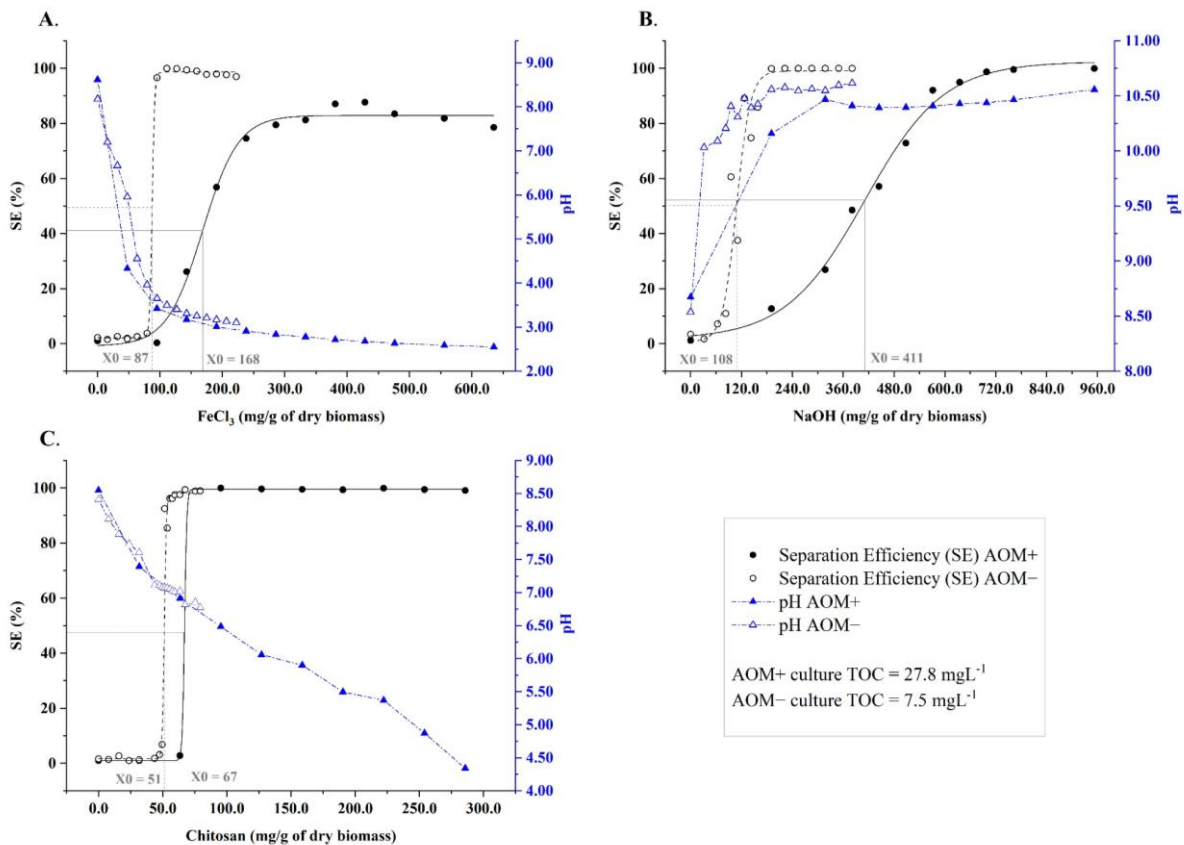
277 ($\text{mg}\cdot\text{L}^{-1}$) corresponding to the maximum SE (A_2 in sigmoidal regression) for each flocculant is

278 presented in Table 1. For all sigmoidal regression fitting, p-values for the t-test of parameters A_2 and

279 x_0 were statistically significant ($p < 0.001$), indicating that these parameters are unlikely to be zero.

280 The optimum flocculant dosages obtained here are selected as a reference dosage for further jar

281 tests.



282

283 **Figure 3:** Dose-response curves (SE% corresponding to an applied dosage of **A.** FeCl₃, **B.** NaOH, and **C.**
 284 Chitosan) from sigmoidal regression of AOM+ vs. AOM- culture jar tests (Jar test set 1). Final pH
 285 values corresponding to applied dosages are represented on the right axis (blue). Highlighted values
 286 indicate the inflection point dosages (x_0) corresponding to grey dashed droplines.
 287

288 Flocculation was successful for all three flocculants, achieving SE above 97%, except for the FeCl₃ in
 289 the AOM+ culture, which achieved 87%. The significant difference ($p < 0.05$) in dose-response
 290 between AOM+ and AOM- cultures is clearly observed in the inflection point dosage (x_0). Since
 291 flocculant dosage is crucial in determining the final cost of flocculation-based harvesting, even the
 292 small change in x_0 and, consequently, the optimum dosage should not be overlooked (Lama et al.,
 293 2016; McGrath et al., 2024). A variation (% decrease) of x_0 in AOM+ versus AOM- culture is highest
 294 for NaOH (74%), followed by FeCl₃ (48%) and chitosan (23%). Prevalence of organic matter in AOM+
 295 culture is indicated by significantly higher TOC concentrations ($27.8 \pm 3.2 \text{ mg} \cdot \text{L}^{-1}$) compared to AOM-
 296 culture ($7.5 \pm 0.8 \text{ mg} \cdot \text{L}^{-1}$) and BG-11 medium ($1.43 \pm 0.12 \text{ mg} \cdot \text{L}^{-1}$). Thus, the disparity observed in the
 297 flocculation dose-response can be attributed to the presence of organic matter, represented in this

298 study as AOM, which is consistent with previous studies (Beuckels et al., 2013; Chen et al., 2009;
 299 Garzon-Sanabria et al., 2013; Wu et al., 2012; Zang et al., 2020; Zhang et al., 2012).

300 **Table 1:** Optimum flocculant dosage (minimum dosage corresponding to maximum SE%), final pH,
 301 and sigmoidal regression parameters (x_0 , dx) from AOM+ vs. AOM- culture dose-response curves (for
 302 each sigmoidal regression, $R^2 = 1.00$).

Flocculants	FeCl ₃		NaOH		Chitosan	
	AOM+	AOM-	AOM+	AOM-	AOM+	AOM-
Dosage (mg g ⁻¹ of dry biomass)	404.8±33.7	119.0±11.2	730.2±44.9	206.3±22.4	111.1±22.4	61.5±2.8
Dosage (mg·L ⁻¹)	255.0±21.2	75.0±7.1	460.0±28.3	130.0±14.1	70.0±14.1	38.8±1.8
Maximum SE (%)	87	99	99	99	99	98
Final pH	2.70±0.03	3.45±0.07	10.45±0.02	10.57±0.01	6.27±0.30	6.89±0.01
x_0 (mg g ⁻¹ of dry biomass)	168.1±5.2	87.4±1.0	410.5±11.6	108.0±5.8	67.0±0.4	51.3±0.5
Slope factor, dx	28.7±4.3	2.0±0.3	93.3±11.1	16.5±4.3	0.9±0.0	0.8±0.2

303 *Culture properties: Initial pH = 8.50, Dry weight = 0.63 g·L⁻¹, AOM+ culture TOC = 27.8±3.2 mg·L⁻¹,
 304 AOM- culture TOC = 7.5±0.8 mg·L⁻¹

305
 306 In the case of FeCl₃ flocculation, the optimum dosage is significantly higher for AOM+ culture (405 mg
 307 g⁻¹ dry biomass) than for AOM- culture (119 mg g⁻¹). The higher dosage requirement for AOM+
 308 culture is also reflected by the slope of the dose-response curve (Figure 3A). From sigmoidal
 309 regression, slope factors (dx) of 28.71 and 2.01 were obtained for AOM+ and AOM- culture,
 310 respectively (Table 1). A large dx indicates lower sensitivity of the sigmoidal curve, requiring higher
 311 dosage change to achieve a quick shift in SE. Conversely, in a higher sensitivity (dx approaching 1)
 312 sigmoidal curve, SE changes rapidly with small dosage increments, as observed for the AOM- dose-
 313 response curve (Figure 3A). During FeCl₃ flocculation, dissolved iron species (such as Fe³⁺, Fe(OH)²⁺,
 314 and Fe(OH)₂⁺) and ferric hydroxide precipitate (Fe(OH)₃) surfaces are cationic at pH < 8.0 (Wyatt et
 315 al., 2012). In the pH range from 4.1 to 8.0, Fe(OH)₂⁺ is the predominant species in equilibrium with

316 positively charged ferric hydroxide precipitate (Johnson & Amirtharajah, 1983). Positively charged
317 precipitates induce flocculation by bridging negatively charged cells together through an electrostatic
318 patch mechanism (Wyatt et al., 2012). Whereas, at high cell concentrations ($> 0.5 \text{ g}\cdot\text{L}^{-1}$), flocculation
319 is induced by the combination of electrostatic bridging and sweep flocculation (Kim et al., 2015;
320 Wyatt et al., 2012). The higher dosage requirement for AOM+ culture could be attributed to the
321 metal complexation properties of AOM, making cationic hydrolyzed species less available for
322 interaction with cells (Chen et al., 2009; Naveed et al., 2019). Since culture pH is not adjusted during
323 the flocculation experiment, FeCl_3 hydrolysis releases hydrogen ions into the culture suspension,
324 causing the pH to decrease from 8.50 to 2.70–3.45 (Table 1). For both AOM+ and AOM– cultures, the
325 pH decreases sharply with increasing FeCl_3 dosage up to $\sim 130 \text{ mg g}^{-1}$ and then shows a plateau at
326 higher dosages (Figure 3A). As observed in previous studies, the final pH corresponding to the
327 maximum SE for both cultures is in the acidic range of 2.70–3.45 (Kim et al., 2015).

328 For NaOH/alkaline flocculation, optimum NaOH dosage at maximum SE (99 %) is 3.5 times higher in
329 the AOM+ culture compared to the AOM– culture. The dose-response curves displayed a trend
330 similar to that observed in FeCl_3 flocculation. The large slope factors ($dx = 93.32$ AOM+ and 16.48 for
331 AOM– cultures) indicate lower sensitivity, requiring higher dosage changes to attain rapid variations
332 in SE (Figure 3B). Since the final pH required to achieve maximum SE for both cultures reaches
333 around 10.50 (Table 1), a larger quantity of NaOH was consumed to reach this pH for the AOM+
334 culture. This is demonstrated by the swift rise in pH with a small NaOH dosage increment in the
335 AOM– culture (Figure 3B). The presence of AOM consumed a significant amount of hydroxide (OH^-)
336 to reach pH 10.50, necessitating additional hydroxide to form $\text{Mg}(\text{OH})_2$ precipitates in the AOM+
337 culture (Besson & Guiraud, 2013; Li et al., 2021; Vandamme et al., 2016). Optimum pH of ≥ 10.50 is
338 reported to be critical for forming gelatinous, positively charged $\text{Mg}(\text{OH})_2$ precipitates, which induce
339 flocculation by charge neutralization and sweep flocculation (Brady et al., 2014; Vandamme et al.,
340 2016). Additionally, Mg^{2+} ions adsorbed on the cell surface at high pH could provide the nucleation

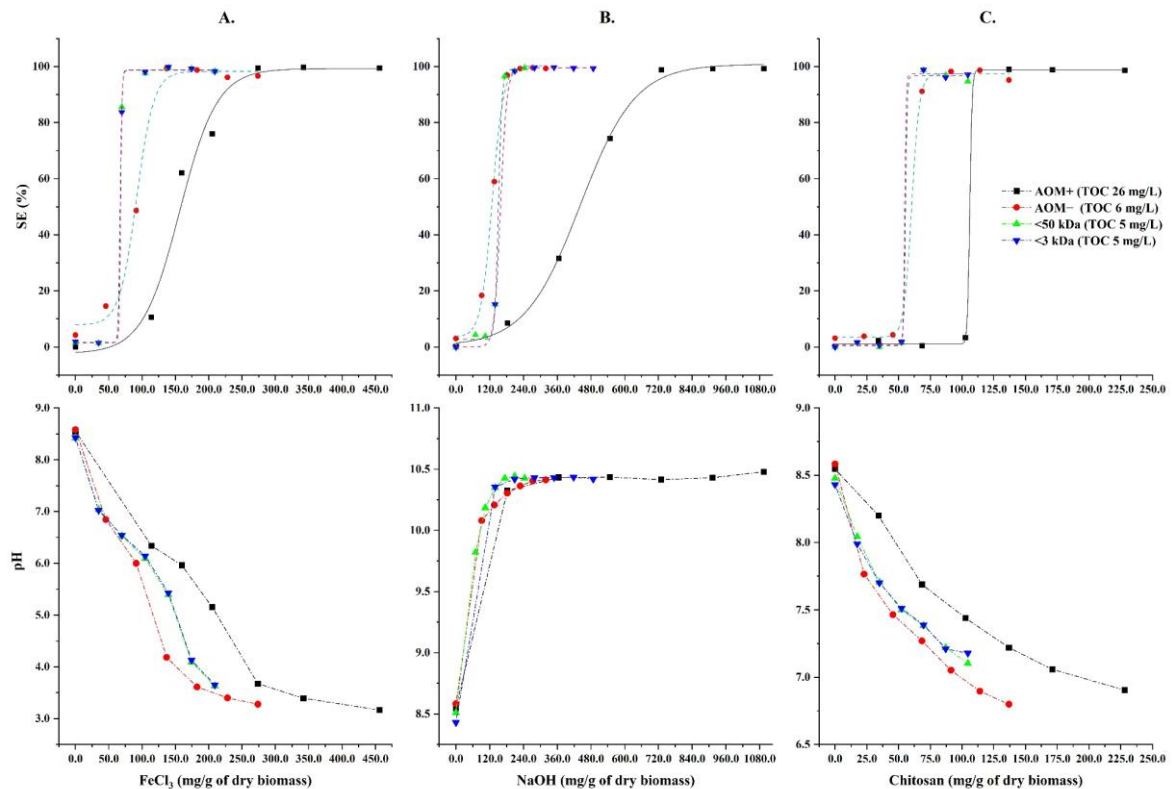
341 sites for $\text{Mg}(\text{OH})_2$ precipitates around the cell, thus enhancing flocculation (Brady et al., 2014; Li et
342 al., 2021). Alkaline pH above 8.50 can also facilitate the formation of calcium phosphate precipitates,
343 promoting sweep flocculation at high concentrations of Ca^{2+} (0.85 mM) and PO_4^{3-} (0.35 mM)
344 (Beuckels et al., 2013; Brady et al., 2014). However, low concentrations of Ca^{2+} (0.24 mM) and PO_4^{3-}
345 (0.05 mM) in this study rule out this possibility. Moreover, at a pH range of 10.50, dominant surface
346 functional groups such as carboxyl (pK_a 2–6), phosphoryl (pK_a 5.6–7.2), and hydroxyl (pK_a 8–12) may
347 remain fully deprotonated (Brady et al., 2014), explaining the relatively high NaOH dosages required
348 compared to FeCl_3 (Figure 3) (Wu et al., 2012).

349 Among the three flocculants, chitosan performed the most efficiently, achieving $\text{SE} \geq 98\%$ at the
350 lowest concentrations of 111 mg g^{-1} dry biomass for AOM+ and 62 mg g^{-1} for AOM– culture.
351 Consistent with FeCl_3 and NaOH flocculation, a higher dosage was required for AOM+ culture
352 compared to AOM– culture. However, the optimum dosage difference between AOM+ and AOM–
353 cultures was minimal. At pH 8.0, it is proposed that no specific/electrostatic interaction occurs
354 between chitosan and cells, and flocculation is primarily induced by a sweeping mechanism (Demir et
355 al., 2020). Thus, the minimal dosage difference observed for AOM+ and AOM– cultures could be
356 attributed to the dominant sweeping mechanism. However, the higher dosage requirement for
357 AOM+ culture, possibly due to intermolecular interaction between chitosan ($\text{pK}_a \sim 6.5$) and
358 deprotonated carboxyl/phosphoryl functional groups in AOM, should not be neglected (Garzon-
359 Sanabria et al., 2013; Zang et al., 2020). Additionally, the sensitivity of the chitosan dose-response
360 curve is approximately identical for both cultures (slope factors, $dx = 0.88$ for AOM+ and 0.80 AOM–)
361 and significantly better (dx approaching 1) than those observed for FeCl_3 and NaOH (Figure 3). pH
362 decrease of both cultures with increasing chitosan dosages follows a consistent trajectory, arriving at
363 a final pH of 6.27 (AOM+) and 6.89 (AOM–) at the maximum SE. Overall, despite the unique
364 mechanism of each flocculant studied, the need for higher dosage is prominent in the presence of

365 AOM. Consequently, further jar tests were conducted to determine the specific AOM fraction
366 accountable for the inhibition.

367 3.3 Interference of AOM permeate (<50 kDa and <3 kDa) fractions in flocculation (Jar test set 2)

368 Sequential ultrafiltration produced two different AOM permeate fractions (8.0 L each): <50 kDa
369 fraction of low/medium- molecular weight (MW) and <3 kDa fraction of low- MW. Jar tests (set 2)
370 evaluated culture suspensions prepared with different AOM fractions: AOM+, AOM-, <50 kDa, and
371 <3 kDa AOM. A maximum SE of $\geq 97\%$ was achieved for all the culture suspensions (Figure 4, first
372 row). The general trend of requiring higher dosage for AOM+ compared to AOM- culture was
373 analogous to the previous jar test set 1 (Figure 3). The optimum dosages and inflection point dosages
374 (x_0) for AOM+ and AOM- cultures are relatively proportional to those in jar test set 1, except for
375 chitosan, which exhibited slightly higher values (see supplementary material, Table S1). The pH
376 response of the culture suspensions to applied flocculant dosages displayed a comparable
377 progression to that in jar test set 1 (Figure 4, second row). The final pH range corresponding to the
378 maximum SE was 3.41–3.89 for FeCl₃, 10.39–10.44 for NaOH, and 6.97–7.27 for chitosan (see
379 supplementary material, Table S1). The marginal disparity in optimum dosages and final pH values
380 for AOM+ and AOM- culture compared to jar test set 1 could be attributed to the cells and AOM
381 being at different growth days.



382

383 **Figure 4:** First row: Dose-response curves (SE% corresponding to an applied dosage of **A.** FeCl₃, **B.**
 384 NaOH, and **C.** Chitosan) from sigmoidal regression of resuspension jar tests with AOM permeate
 385 fractions (Jar test set 2). Second row: Final pH values corresponding to applied dosages. For each
 386 sigmoidal regression, $R^2 = 1.00$.

387

388 The most critical observation is the approximately synchronized dose responses of <50 kDa and <3

389 kDa AOM culture suspensions with the AOM- culture. Except for the subtle variation in FeCl₃

390 flocculation of AOM- culture, the dose-response and pH change trajectories followed a consistent

391 pattern. This observation indicates that low to medium MW (<3 kDa and <50 kDa) AOM fractions are

392 less likely to be primary contributors to flocculation inhibition. Low TOC contents (5–6 mg·L⁻¹) of

393 AOM-, <50 kDa and <3 kDa AOM culture suspensions support the synchronizing dose-response

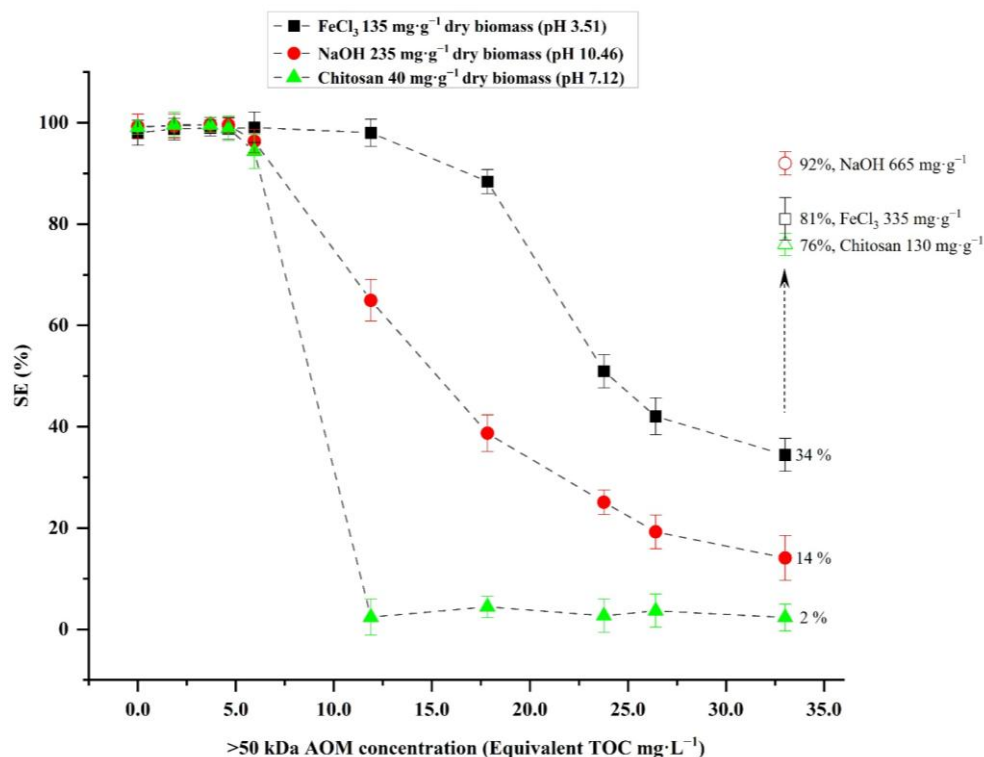
394 curves, in contrast to AOM+ culture (26 mg·L⁻¹). Thus, the majority of the flocculation-inhibiting

395 substances are likely in the high MW (>50 kDa) AOM fraction. To confirm this hypothesis, further jar

396 tests (set 3) were carried out with the concentrated AOM retentate fraction.

397 **3.4 Interference of AOM retentate (>50 kDa) fraction in flocculation (Jar test set 3)**

398 Two different concentrated AOM retentate fractions (~0.7 L each) of >50 kDa (high- MW) and 3–50
399 kDa (medium- MW) were obtained after the sequential ultrafiltration. Since jar test set 2
400 demonstrated that <50 kDa AOM fraction is not primarily responsible for flocculation inhibition,
401 detailed jar tests with 3–50 kDa AOM retentate fraction were not included (also confirmed with
402 preliminary jar tests, data not included). Thus, jar tests (set 3) were carried out only with >50 kDa
403 AOM fraction. AOM– culture control tests achieved SE of $\geq 98\%$ for each flocculant at a given
404 optimum dosage, with corresponding pH of 3.5, 10.5, and 7.1 for FeCl_3 , NaOH, and chitosan,
405 respectively (Figure 5). SE ($\geq 98\%$) remained unaffected till the addition of >50 kDa AOM up to 5
406 $\text{mg}\cdot\text{L}^{-1}$ (TOC equivalent concentration). However, with increasing concentration of >50 kDa AOM, SE
407 decreased for all three flocculants. Flocculation by chitosan was impacted most with complete
408 inhibition (SE reduced to 2%), followed by NaOH (14%) and FeCl_3 (34%) at a TOC concentration of 33
409 $\text{mg}\cdot\text{L}^{-1}$. This TOC level can typically be reached in early stationary phase culture (Figure 2B). The
410 flocculation inhibition effect can be alleviated by increasing the flocculant dosage; however,
411 complete restoration of SE ($\geq 98\%$) was not observed at the given final flocculant dosages (increased
412 SE % for the final treatment, open symbols above dashed arrow, Figure 5). The final pH after
413 increased dosing did not change significantly. From the AOM fractions jar tests (sets 2 and 3), it is
414 clear that high molecular weight >50 kDa AOM fraction is primarily accountable for flocculation
415 interference, demanding higher flocculant dosage. Such inhibition by higher molecular weight AOM
416 has also been suggested in previous studies by Bernhardt et al. (>2 kDa) (Bernhardt et al., 1991),
417 Vandamme et al. (>3 kDa) (Vandamme et al., 2016), Takaara et al. (>10 kDa) (Takaara et al., 2010),
418 and Yang (>50 kDa) (Yang et al., 2020).



419

420 **Figure 5:** Dose-response (SE %) at increasing concentrations of >50 kDa AOM using optimum
 421 flocculant dosage in AOM- culture (resuspension jar test set 3). Individually labeled SE % for the final
 422 treatment (open symbols above dashed arrow) represents the increased SE after adding extra
 423 flocculant dosage up to the final concentration, as mentioned in the data points.

424

425 As observed from the jar test series, AOM demands a high flocculant dosage, suggesting an
 426 interaction between flocculants and AOM (Fan et al., 2017; Pivokonsky et al., 2012; Vandamme et al.,
 427 2016; Zang et al., 2020; Zhang et al., 2012). This interaction was indirectly assessed by measuring the
 428 removal (%) of supernatant TOC, Fe³⁺ and Mg²⁺ relative to the control culture and AOM (Chen et al.,
 429 2009; Fan et al., 2017; Vandamme et al., 2016; Wu et al., 2012). Jar tests were performed on AOM+
 430 culture and AOM only, using optimum flocculant dosages (Table 2). TOC removal was highest for
 431 NaOH flocculation. The comparable removal of TOC and Mg²⁺ for both culture and AOM suggests
 432 dominant sweep flocculation, which removes both cells and AOM collectively. FeCl₃ flocculation
 433 showed the lowest TOC removal; however, Fe³⁺ removal was higher in culture (52 %) compared to
 434 AOM (29 %). Higher Fe³⁺ removal could be due to the direct/stronger interaction of Fe ions (in

435 cationic hydrolyzed species) with the cells compared to AOM. For chitosan flocculation, TOC removal
 436 (%) was calculated after subtracting the TOC contributed by the corresponding chitosan dosage, and
 437 the removal was higher than that observed for FeCl₃. In general, the removal of TOC/flocculant is
 438 varied broadly, indicating different mechanisms and degrees of interaction. Therefore, to discern the
 439 interaction dynamics of AOM and different flocculants, it is crucial to analyze the AOM composition
 440 and their major active functional groups in the given physiochemical environment (pH, salinity, ionic
 441 strength, etc.) (Henderson et al., 2008; Pivokonsky et al., 2012; Zang et al., 2020; Zhang et al., 2012).

442 **Table 2:** Jar test supernatant flocculant-AOM removal (%) measured in terms of TOC, Fe³⁺, and Mg²⁺.

Treatments*	Supernatant TOC removal (%)	Supernatant Fe ³⁺ or Mg ²⁺ removal (%)	SE (%)
AOM+ culture + FeCl ₃	15	52	89
AOM+ culture + NaOH	64	58	98
AOM+ culture + Chitosan	62	NA	98
AOM only + FeCl ₃	22	29	NA
AOM only + NaOH	67	59	NA
AOM only + Chitosan	49	NA	NA

443 *Flocculant Dosage: FeCl₃ 200 mg·L⁻¹, NaOH 480 mg·L⁻¹ (+10 mM Mg²⁺), Chitosan 75 mg·L⁻¹, Culture
 444 dry biomass concentration: 0.60 g·L⁻¹, Culture TOC = 36.5±1.2 mg·L⁻¹, NA: not applicable
 445

446 3.5 Compositional analysis of AOM retentate (>50 kDa) fraction

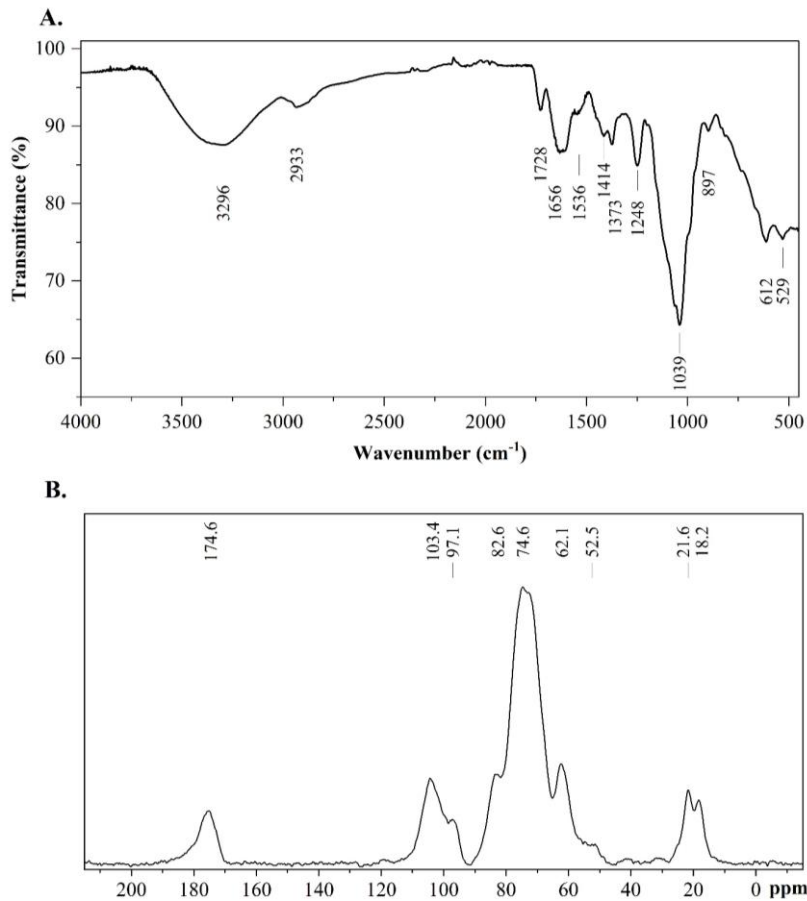
447 The interference of AOM in the flocculation process could arise from competition between net
 448 negatively charged cells and AOM for positively charged flocculants or from complex formation,
 449 depending on the composition of AOM (Cheng et al., 2022; Naveed et al., 2019; Pivokonsky et al.,
 450 2012; Zang et al., 2020; Zhang et al., 2012). Since >50 kDa AOM fraction is primarily responsible for
 451 flocculation interference, its composition was first analyzed using non-destructive techniques (FTIR,
 452 ¹³C-CP/MAS NMR) to identify the major functional groups in their native state. Subsequently, acid-
 453 hydrolyzed AOM was used for monosaccharide composition analysis using HPAEC-PAD.

454 3.5.1 FTIR analysis of >50 kDa AOM fraction

455 The FTIR spectrum of >50 kDa AOM revealed characteristics indicative of abundant polysaccharides,
456 as evidenced by intense bands in the 1200–900 cm^{-1} region (Figure 6A) (Barborikova et al., 2019;
457 Cybulska et al., 2016; Liu et al., 2021). A broad band around 3296 cm^{-1} , encompassing both O–H and
458 N–H stretching, along with aliphatic sidechain CH_2 stretching at 2933 cm^{-1} , is typical of hydrophilic
459 polysaccharides (Barborikova et al., 2019; Cybulska et al., 2016; Villacorte et al., 2015). A major peak
460 at 1039 cm^{-1} denotes C–O stretch and C–O–H in-plane bending vibrations of the pyranose ring in the
461 polysaccharide (Cybulska et al., 2016). A small peak at 897 cm^{-1} suggests β configuration (C1–H
462 bending) of glycosidic linkages. The bands in the region 735–450 cm^{-1} represent C–C stretch skeletal
463 vibrations (Liu et al., 2021).

464 A sharp peak at 1248 cm^{-1} signifies the key properties of polysaccharides from the bending vibrations
465 of C–O–H and C–C in carboxylic acid/ester moieties. Two small peaks at 1373 cm^{-1} and 1414 cm^{-1}
466 represent the bending and wagging of CH and CH_2 groups of polysaccharides, respectively. A
467 relatively broad peak in the region 1656–1536 cm^{-1} is characteristic of carboxylate C=O and N–H
468 deformations of amide I/II of glycan N–acetyl groups and protein secondary structure. Since >50 kDa
469 AOM is richer in carbohydrates (42 wt.%) than proteins (23 wt. %), the amide I/II bands are plausibly
470 due to the glycoprotein nature of the AOM.

471 The prominent peak at 1728 cm^{-1} indicates the C=O stretch of the protonated carboxylic group (–
472 COOH) from uronic acids (Capek et al., 2008). This unique –COOH peak is absent in 3–50 kDa AOM
473 fraction (see supplementary material, Figure S1), aligning with the jar test (set 2) observation that
474 there was no flocculation inhibition in <50 kDa AOM resuspension culture (Figure 4). In contrast,
475 inhibition was clearly observed (jar test set 3) with >50 kDa AOM containing –COOH peak (Figure 5).
476 Overall, >50 kDa AOM is a complex glycan with a unique presence of carboxyl–bearing uronic or sialic
477 acids (Capek et al., 2008; Pinel et al., 2020).



478

479 **Figure 6: A.** FTIR spectrum and **B.** ¹³C-CP/MAS NMR spectrum of >50 kDa AOM fraction.

480

481 3.5.2 Solid-state ¹³C-NMR spectroscopy analysis of >50 kDa AOM fraction

482 The ¹³C-CP/MAS NMR spectrum of >50 kDa AOM is shown in Figure 6B. The broad resonance signals
483 in the 60–110 ppm range originate from the different carbon units (C1–C6) of hexose sugar,

484 **indicating** the presence of high molecular weight glycans (Capek et al., 2008). **A conspicuous** signal at
485 174.6 ppm is attributed to carbonyl carbons (C=O) from N-acetylamino groups as well as to the

486 carboxylic acid (–COOH) functional group of uronic and sialic acid monomer units in glycan (Arnold et
487 al., 2015; Capek et al., 2008; Kang et al., 2018; Perez Garcia et al., 2011). **A peak** at 103.4 ppm

488 corresponds to the β-anomeric carbons (C1) involved in glycosidic linkages (O–C–O functionalities) of
489 monomer units such as glucose and galactose. **A small** shoulder peak at 97.1 represents α-anomeric

490 C1 carbons from monomer units such as xylose, rhamnose, galacturonic acid, etc. (Arnold et al.,
491 2015; Perez Garcia et al., 2011; White et al., 2014).

492 A broad peak between 60–85 ppm covers the different carbon units (C2, C3, C4, C5, and C6) of the
493 monomer units (Perez Garcia et al., 2011; Poulhazan et al., 2021). An intense peak at 74.6 ppm
494 corresponds to the C2/C5 carbons, with a shoulder peak at 82.6 ppm due to C3/C4 carbons. The
495 distinct peak at 62.1 ppm arises due to hydroxymethyl carbons $\underline{\text{C}}\text{H}_2\text{OH}$ (C6). A small indistinct
496 shoulder signal at 52.5 ppm can be attributed to a methoxyl carbon ($-\text{COO}\underline{\text{C}}\text{H}_3$), such as the ester
497 methoxy group attached to carbonyl carbon (C6) of galacturonic acid. The peaks in the 15–36 ppm
498 region are generally assigned to aliphatic sidechains (CH_3 , CH_2 , and CH) of lipids and proteins
499 (Poulhazan et al., 2021; White et al., 2014). However, absence of strong signals from sp^2 hybridized
500 carbon in the region 110–160 ppm (due to aromatic amino acids and unsaturated C=C bonds in lipids
501 and fatty acids) implies that the aliphatic signals are most likely from methyl carbons ($\underline{\text{C}}\text{H}_3$) of glycan
502 monomers (Capek et al., 2008; Mathieu-Rivet et al., 2020; Perez Garcia et al., 2011; Poulhazan et al.,
503 2021).

504 A peak at 21.6 ppm (combined with the carbonyl (C=O) peak at 174.6 ppm) can be assigned to methyl
505 carbons from acetyl groups ($-\text{CO}\underline{\text{C}}\text{H}_3$), such as the acetyl CH_3 of N-acetylglucosamine. Generally, the
506 core of N-glycans contains two residues of N-acetylglucosamine, which, along with other residues in
507 the glycan structure, could be the origin of the acetyl CH_3 signal (Capek et al., 2008; Mathieu-Rivet et
508 al., 2020; Perez Garcia et al., 2011; White et al., 2014). The small shoulder at 18.2 ppm represents the
509 methyl carbons ($-\underline{\text{C}}\text{H}_3$) from 6-deoxy sugars (e.g., C6 of rhamnose and fucose) (Capek et al., 2008;
510 White et al., 2014). Thus, >50 kDa AOM fraction is a high molecular weight complex glycan with
511 carboxyl ($-\text{COOH}$) and N-acetylamino ($-\text{NHCOCH}_3$) group-bearing monomers.

512 **3.5.3 Total carbohydrate, total protein, and monosaccharides composition of >50 kDa AOM**
513 **fraction**

514 The total carbohydrate and protein contents of >50 kDa AOM were 42% and 23% on a lyophilized dry
515 weight basis (wt %), respectively, indicating its glycoprotein nature (Capek et al., 2008; Rao et al.,
516 2020). Moisture and ash content were 6 wt % and 9 wt %, as determined via thermogravimetric
517 analysis. HPAEC–PAD-based analysis of monosaccharides after acid hydrolysis shows that the AOM is
518 a heteropolysaccharide composed of neutral, amino, and acidic sugars (see supplementary material,
519 Figure S2). Quantified monosaccharides consisted of arabinose (30.05 wt %), glucosamine (6.58 wt
520 %), glucose (4.17 wt %), xylose (3.02 wt %), mannose (3.81 wt %), and glucuronic acid (1.75 wt %).
521 Trace amounts of rhamnose (retention time, RT=9.8 min) and galactose were detected but not
522 quantified due to the low peak area. Fucose and ribose were not present in the AOM. One small peak
523 in the neutral sugar region (RT=11.7 min) was not identified. In addition to traces of galacturonic
524 acid, a major unidentified peak in the acidic sugar region (RT=35.8 min) is most likely of N–
525 acetylneuraminic acid (Neu5Ac), a prominent sialic acid typically present as a terminal sugar in the
526 glycoprotein complexes (Capek et al., 2008; Cybulska et al., 2016; Mathieu-Rivet et al., 2020; Pinel et
527 al., 2020). The presence of acidic sugars confirms the carboxyl functional groups (–COOH) in the
528 AOM, which were also detected in the FTIR and ¹³C–CP/MAS NMR spectra.

529 **3.6 Potential functional group(s) responsible for flocculation inhibition based on the**
530 **compositional analysis**

531 Overall compositional analyses of >50 kDa AOM fraction illustrated that it is a high molecular weight
532 heteropolysaccharide composed of neutral, amino, and acidic sugars. Among various functional
533 groups, the carboxyl group (–COOH) from acidic monomers– prominently observed in this study– is
534 particularly important from the flocculation perspective. The interaction of surface-active carboxyl
535 groups with cationic flocculants could occur through ion exchange, complexation, or precipitation
536 (Kaplan et al., 1987; Naveed et al., 2019). Thus, competition between cell–surface and AOM carboxyl
537 groups for the flocculant, leading to a higher dosage requirement, is a well-observed phenomenon in

538 this and other studies (Brady et al., 2014; Cheng et al., 2022; Pivokonsky et al., 2012; Vandamme et
539 al., 2016; Zang et al., 2020; Zhang et al., 2012).

540 A recent study by Cheng *et al.* suggested a low suspension pH to prevent the deprotonation of the
541 carboxyl group to reduce the inhibitory effect of carboxyl groups (Cheng et al., 2022). In this study,
542 even though the optimum pH was in the acidic range (2.70–3.45 at maximum SE %) for FeCl₃
543 flocculation, the AOM inhibitory effect was still present (Figures 3 and 4), indicating strong inhibitory
544 effects of the carboxyl group. In comparison, a much higher inhibitory effect was observed for the
545 NaOH flocculation at pH 10.5. At alkaline pH, deprotonated carboxyl groups of AOM may chelate
546 Mg²⁺ ions, demanding higher NaOH dosages to induce Mg(OH)₂ precipitate formation (Besson &
547 Guiraud, 2013; Brady et al., 2014; Vandamme et al., 2016). Additionally, deprotonated phosphoryl
548 and hydroxyl groups could amplify Mg²⁺ chelation, inducing a stronger inhibitory effect compared to
549 acidic pH conditions in FeCl₃ flocculation (Figures 3, 4, and 5) (Besson & Guiraud, 2013; Fan et al.,
550 2017; Vandamme et al., 2016; Wu et al., 2012). Moreover, the optimum chitosan flocculation (SE ≥98
551 %) occurred in the neutral pH region (6.25–7.25, Figures 3 and 4), where carboxyl groups (pK_a 2–6)
552 mostly remained deprotonated (Pivokonsky et al., 2012). The strong polarity of the deprotonated
553 carboxyl groups can induce high electrostatic interactions (coordinate bonds) with positively charged
554 amine (–NH₃⁺) functional groups of chitosan (pK_a ~ 6.5) (Zang et al., 2020). This could explain the
555 significantly higher inhibition tendency of chitosan by >50 kDa AOM compared to FeCl₃ or NaOH
556 flocculation (Figure 5).

557 For all the flocculants used in this study, AOM interference was due to a high molecular weight (>50
558 kDa) fraction. Thus, interfering functional groups such as carboxyl, phosphoryl, amine, and hydroxyl
559 should be associated with the polysaccharide complex rather than small molecular weight oligo- or
560 monosaccharides. Studies on model AOM demonstrated that only the polymeric molecule (alginate),
561 not the monosaccharides, had an inhibitory effect on flocculation (Beuckels et al., 2013; Cheng et al.,
562 2022; Vandamme et al., 2016). In this study, AOM used mainly comprised cell-secreted soluble

563 extracellular organic matter. Generally, as in other microorganisms, microalgal extracellular organic
564 matter is also secreted as a glycoconjugate complex performing various cellular functions such as
565 substrate adhesion, nutrient retention, and protection against dehydration, predatory microbes or
566 harmful chemicals, etc. (Mathieu-Rivet et al., 2020; Rao et al., 2020; Zhou et al., 2024). Most of this
567 secreted extracellular matter consists of glycoproteins with diverse compositions and proportions of
568 glycan monomer (Mathieu-Rivet et al., 2020; Rao et al., 2020). Based on the total
569 carbohydrate/protein and monosaccharide compositions in this study, it is conceivable that the AOM
570 is structured as a glycoprotein, potentially featuring either N-glycan with xylosylated core (N-
571 acetylglucosamine2, Man3) or O-glycan with sialic acid terminal (Capek et al., 2008; Mathieu-Rivet et
572 al., 2020; Pinel et al., 2020; Rao et al., 2020). Thus, further studies on glycosidic linkage and
573 glycoprotein genomics/proteomics are needed to elucidate the AOM structure and the
574 conformational state of active functional groups interfering with the flocculation process.

575

576

577 **4 Conclusion**

578 This study demonstrates that the >50 kDa AOM fraction is primarily responsible for the inhibition of
579 *Chlorella* sp. flocculation induced by FeCl₃, NaOH, and chitosan., requiring increased flocculant
580 dosages. The presence of carboxyl groups (-COOH) from acidic monomers in AOM plays a crucial role
581 in this inhibition, particularly under varying pH conditions. Compositional analysis confirmed that
582 AOM is a high molecular weight glycoprotein rich in carbohydrates. These findings highlight the
583 importance of understanding AOM composition and interactions with flocculants to optimize
584 flocculation processes. Further research on glycosidic linkages and glycoprotein structures is
585 recommended to mitigate AOM's inhibitory effects.

586

587 **References:**

- 588 Ajala, S.O., Alexander, M.L. 2020. Assessment of *Chlorella vulgaris*, *Scenedesmus obliquus*, and
589 *Oocystis minuta* for removal of sulfate, nitrate, and phosphate in wastewater. *International Journal*
590 *of Energy and Environmental Engineering*, **11**(3), 311-326.
- 591 Arnold, A.A., Genard, B., Zito, F., Tremblay, R., Warschawski, D.E., Marcotte, I. 2015. Identification of
592 lipid and saccharide constituents of whole microalgal cells by (1)(3)C solid-state NMR. *Biochim*
593 *Biophys Acta*, **1848**(1 Pt B), 369-77.
- 594 Barborikova, J., Sutovska, M., Kazimierova, I., Joskova, M., Franova, S., Kopecky, J., Capek, P. 2019.
595 Extracellular polysaccharide produced by *Chlorella vulgaris* - Chemical characterization and anti-
596 asthmatic profile. *Int J Biol Macromol*, **135**, 1-11.
- 597 Bernhardt, H., Schell, H., Hoyer, O., Lüsse, B. 1991. Influence of algogenic organic substances on
598 flocculation and filtration. *WISA*. pp. 41-57.
- 599 Besson, A., Guiraud, P. 2013. High-pH-induced flocculation-flotation of the hypersaline microalga
600 *Dunaliella salina*. *Bioresour Technol*, **147**, 464-470.
- 601 Beuckels, A., Depraetere, O., Vandamme, D., Foubert, I., Smolders, E., Muylaert, K. 2013. Influence of
602 organic matter on flocculation of *Chlorella vulgaris* by calcium phosphate precipitation. *Biomass and*
603 *Bioenergy*, **54**, 107-114.
- 604 Brady, P.V., Pohl, P.I., Hewson, J.C. 2014. A coordination chemistry model of algal autoflocculation.
605 *Algal Research*, **5**(1), 226-230.
- 606 Capek, P., Matulova, M., Combourieu, B. 2008. The extracellular proteoglycan produced by *Rhodella*
607 *grisea*. *Int J Biol Macromol*, **43**(4), 390-3.
- 608 Chen, L., Li, P.F., Liu, Z.L., Jiao, Q.C. 2009. The released polysaccharide of the cyanobacterium
609 *Aphanothece halophytica* inhibits flocculation of the alga with ferric chloride. *Journal of Applied*
610 *Phycology*, **21**(3), 327-331.
- 611 Cheng, S., Zhang, H., Li, L., Yu, T., Wang, Y., Tan, D., Zhang, X. 2022. Harvesting of *Microcystis flos-*
612 *aquae* using dissolved air flotation: The inhibitory effect of carboxyl groups in uronic acid-containing
613 carbohydrates. *Chemosphere*, **300**, 134466.
- 614 Cheng, S., Zhang, H., Wang, H., Mubashar, M., Li, L., Zhang, X. 2024. Influence of algal organic matter
615 in the in-situ flotation removal of *Microcystis* using positively charged bubbles. *Bioresour Technol*,
616 **397**, 130468.
- 617 Cybulska, J., Halaj, M., Cepák, V., Lukavsky, J., Capek, P. 2016. Nanostructure features of microalgae
618 biopolymer. *Starch-Starke*, **68**(7-8), 629-636.
- 619 Demir, I., Blockx, J., Dague, E., Guiraud, P., Thielemans, W., Muylaert, K., Formosa-Dague, C. 2020.
620 Nanoscale Evidence Unravels Microalgae Flocculation Mechanism Induced by Chitosan. *ACS Appl Bio*
621 *Mater*, **3**(12), 8446-8459.
- 622 Fan, J., Zheng, L., Bai, Y., Saroussi, S., Grossman, A.R. 2017. Flocculation of *Chlamydomonas*
623 *reinhardtii* with Different Phenotypic Traits by Metal Cations and High pH. *Front Plant Sci*, **8**, 1997.

- 624 Garzon-Sanabria, A.J., Ramirez-Caballero, S.S., Moss, F.E., Nikolov, Z.L. 2013. Effect of algogenic
625 organic matter (AOM) and sodium chloride on *Nannochloropsis salina* flocculation efficiency.
626 *Bioresour Technol*, **143**, 231-7.
- 627 Henderson, R., Parsons, S.A., Jefferson, B. 2008. The impact of algal properties and pre-oxidation on
628 solid-liquid separation of algae. *Water Res*, **42**(8-9), 1827-45.
- 629 Johnson, P.N., Amirtharajah, A. 1983. Ferric chloride and alum as single and dual coagulants. *Journal*
630 *AWWA*, **75**(5), 232-239.
- 631 Kang, X., Kirui, A., Muszynski, A., Widanage, M.C.D., Chen, A., Azadi, P., Wang, P., Mentink-Vigier, F.,
632 Wang, T. 2018. Molecular architecture of fungal cell walls revealed by solid-state NMR. *Nat Commun*,
633 **9**(1), 2747.
- 634 Kaplan, D., Christiaen, D., Arad, S.M. 1987. Chelating Properties of Extracellular Polysaccharides from
635 *Chlorella* spp. *Appl Environ Microbiol*, **53**(12), 2953-6.
- 636 Kim, D.Y., Oh, Y.K., Park, J.Y., Kim, B., Choi, S.A., Han, J.I. 2015. An integrated process for microalgae
637 harvesting and cell disruption by the use of ferric ions. *Bioresour Technol*, **191**, 469-74.
- 638 Lama, S., Muylaert, K., Karki, T.B., Foubert, I., Henderson, R.K., Vandamme, D. 2016. Flocculation
639 properties of several microalgae and a cyanobacterium species during ferric chloride, chitosan and
640 alkaline flocculation. *Bioresour Technol*, **220**, 464-470.
- 641 Li, Y.F., Ma, Q.W., Pan, Y.W., Chen, Q.X., Sun, Z.T., Hu, P. 2021. Development of an effective
642 flocculation method by utilizing the auto-flocculation capability of *Phaeodactylum tricornutum*. *Algal*
643 *Research-Biomass Biofuels and Bioproducts*, **58**, 102413-102413.
- 644 Liu, X., Renard, C., Bureau, S., Le Bourvellec, C. 2021. Revisiting the contribution of ATR-FTIR
645 spectroscopy to characterize plant cell wall polysaccharides. *Carbohydr Polym*, **262**, 117935.
- 646 Liu, Z., Hao, N., Hou, Y., Wang, Q., Liu, Q., Yan, S., Chen, F., Zhao, L. 2023. Technologies for harvesting
647 the microalgae for industrial applications: Current trends and perspectives. *Bioresour Technol*, **387**,
648 129631.
- 649 Mathieu-Rivet, E., Mati-Baouche, N., Walet-Balieu, M.L., Lerouge, P., Bardor, M. 2020. N- and O-
650 Glycosylation Pathways in the Microalgae Polyphyletic Group. *Front Plant Sci*, **11**, 609993.
- 651 McGrath, S.J., Laamanen, C.A., Senhorinho, G.N.A., Scott, J.A. 2024. Microalgal harvesting for biofuels
652 – Options and associated operational costs. *Algal Research*, **77**, 103343-103343.
- 653 Nagel, A., Sirisakulwat, S., Carle, R., Neidhart, S. 2014. An acetate-hydroxide gradient for the
654 quantitation of the neutral sugar and uronic acid profile of pectins by HPAEC-PAD without
655 postcolumn pH adjustment. *J Agric Food Chem*, **62**(9), 2037-48.
- 656 Naveed, S., Li, C.H., Lu, X.D., Chen, S.S., Yin, B., Zhang, C.H., Ge, Y. 2019. Microalgal extracellular
657 polymeric substances and their interactions with metal(loid)s: A review. *Critical Reviews in*
658 *Environmental Science and Technology*, **49**(19), 1769-1802.
- 659 Perez Garcia, M., Zhang, Y., Hayes, J., Salazar, A., Zabolina, O.A., Hong, M. 2011. Structure and
660 interactions of plant cell-wall polysaccharides by two- and three-dimensional magic-angle-spinning
661 solid-state NMR. *Biochemistry*, **50**(6), 989-1000.

662 Pinel, I.S.M., Kleikamp, H.B.C., Pabst, M., Vrouwenvelder, J.S., van Loosdrecht, M.C.M., Lin, Y.M.
663 2020. Sialic Acids: An Important Family of Carbohydrates Overlooked in Environmental Biofilms.
664 *Applied Sciences-Basel*, **10**(21), 7694-7694.

665 Pivokonsky, M., Safarikova, J., Bubakova, P., Pivokonska, L. 2012. Coagulation of peptides and
666 proteins produced by *Microcystis aeruginosa*: Interaction mechanisms and the effect of Fe-
667 peptide/protein complexes formation. *Water Res*, **46**(17), 5583-5590.

668 Poulhazan, A., Dickwella Widanage, M.C., Muszynski, A., Arnold, A.A., Warschawski, D.E., Azadi, P.,
669 Marcotte, I., Wang, T. 2021. Identification and Quantification of Glycans in Whole Cells: Architecture
670 of Microalgal Polysaccharides Described by Solid-State Nuclear Magnetic Resonance. *J Am Chem Soc*,
671 **143**(46), 19374-19388.

672 Qin, S., Wang, K., Gao, F., Ge, B., Cui, H., Li, W. 2023. Biotechnologies for bulk production of
673 microalgal biomass: from mass cultivation to dried biomass acquisition. *Biotechnol Biofuels Bioprod*,
674 **16**(1), 131.

675 Rao, N.R.H., Granville, A.M., Wich, P.R., Henderson, R.K. 2020. Detailed algal extracellular
676 carbohydrate-protein characterisation lends insight into algal solid-liquid separation process
677 outcomes. *Water Res*, **178**, 115833.

678 Shitanaka, T., Fujioka, H., Khan, M., Kaur, M., Du, Z.Y., Khanal, S.K. 2024. Recent advances in
679 microalgal production, harvesting, prediction, optimization, and control strategies. *Bioresour
680 Technol*, **391**(Pt A), 129924.

681 Takaara, T., Sano, D., Masago, Y., Omura, T. 2010. Surface-retained organic matter of *Microcystis
682 aeruginosa* inhibiting coagulation with polyaluminum chloride in drinking water treatment. *Water
683 Res*, **44**(13), 3781-6.

684 Van Wychen, S., Laurens, L.M.L. 2016. Determination of Total Carbohydrates in Algal Biomass:
685 Laboratory Analytical Procedure (LAP).

686 Vandamme, D., Beuckels, A., Vadelius, E., Depraetere, O., Noppe, W., Dutta, A., Foubert, I., Laurens,
687 L., Muylaert, K. 2016. Inhibition of alkaline flocculation by algal organic matter for *Chlorella vulgaris*.
688 *Water Res*, **88**, 301-307.

689 Vandamme, D., Foubert, I., Fraeye, I., Muylaert, K. 2012. Influence of organic matter generated by
690 *Chlorella vulgaris* on five different modes of flocculation. *Bioresour Technol*, **124**, 508-11.

691 Villacorte, L.O., Ekowati, Y., Neu, T.R., Kleijn, J.M., Winters, H., Amy, G., Schippers, J.C., Kennedy,
692 M.D. 2015. Characterisation of algal organic matter produced by bloom-forming marine and
693 freshwater algae. *Water Res*, **73**, 216-30.

694 Vu, H.P., Nguyen, L.N., Emmerton, B., Wang, Q., Ralph, P.J., Nghiem, L.D. 2021. Factors governing
695 microalgae harvesting efficiency by flocculation using cationic polymers. *Bioresour Technol*, **340**,
696 125669.

697 White, P.B., Wang, T., Park, Y.B., Cosgrove, D.J., Hong, M. 2014. Water-polysaccharide interactions in
698 the primary cell wall of *Arabidopsis thaliana* from polarization transfer solid-state NMR. *J Am Chem
699 Soc*, **136**(29), 10399-409.

700 Wu, Z., Zhu, Y., Huang, W., Zhang, C., Li, T., Zhang, Y., Li, A. 2012. Evaluation of flocculation induced
701 by pH increase for harvesting microalgae and reuse of flocculated medium. *Bioresour Technol*,
702 **110**(SUPPL.2), 496-502.

703 Wyatt, N.B., Gloe, L.M., Brady, P.V., Hewson, J.C., Grillet, A.M., Hankins, M.G., Pohl, P.I. 2012. Critical
704 conditions for ferric chloride-induced flocculation of freshwater algae. *Biotechnol Bioeng*, **109**(2),
705 493-501.

706 Yang, L., Zhang, H.Y., Cheng, S.Z., Zhang, W., Zhang, X.Z. 2020. Enhanced Microalgal Harvesting Using
707 Microalgae-Derived Extracellular Polymeric Substance as Flocculation Aid. *Acs Sustainable Chemistry*
708 *& Engineering*, **8**(10), 4069-4075.

709 Zang, X., Zhang, H., Liu, Q., Li, L., Li, L., Zhang, X. 2020. Harvesting of *Microcystis flos-aquae* using
710 chitosan coagulation: Influence of proton-active functional groups originating from extracellular and
711 intracellular organic matter. *Water Res*, **185**, 116272.

712 Zhang, S., Cao, J., Zheng, Y., Hou, M., Song, L., Na, J., Jiang, Y., Huang, Y., Liu, T., Wei, H. 2024. Insight
713 into coagulation/flocculation mechanisms on microalgae harvesting by ferric chloride and
714 polyacrylamide in different growth phases. *Bioresour Technol*, **393**, 130082.

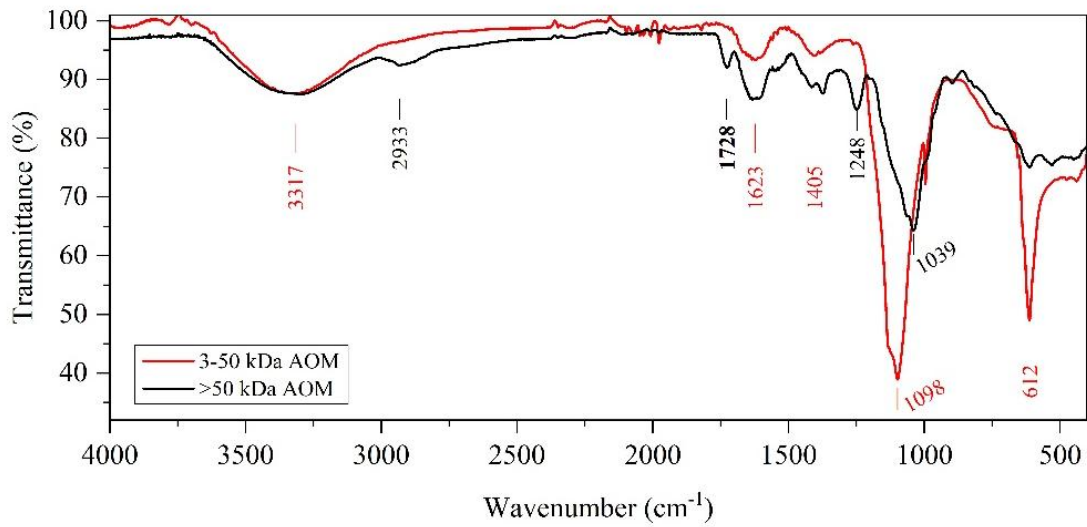
715 Zhang, X., Amendola, P., Hewson, J.C., Sommerfeld, M., Hu, Q. 2012. Influence of growth phase on
716 harvesting of *Chlorella zofingiensis* by dissolved air flotation. *Bioresour Technol*, **116**, 477-84.

717 Zhou, Y., Cui, X., Wu, B., Wang, Z., Liu, Y., Ren, T., Xia, S., Rittmann, B.E. 2024. Microalgal extracellular
718 polymeric substances (EPS) and their roles in cultivation, biomass harvesting, and bioproducts
719 extraction. *Bioresour Technol*, **406**, 131054.

720

721 **Supplementary Material**

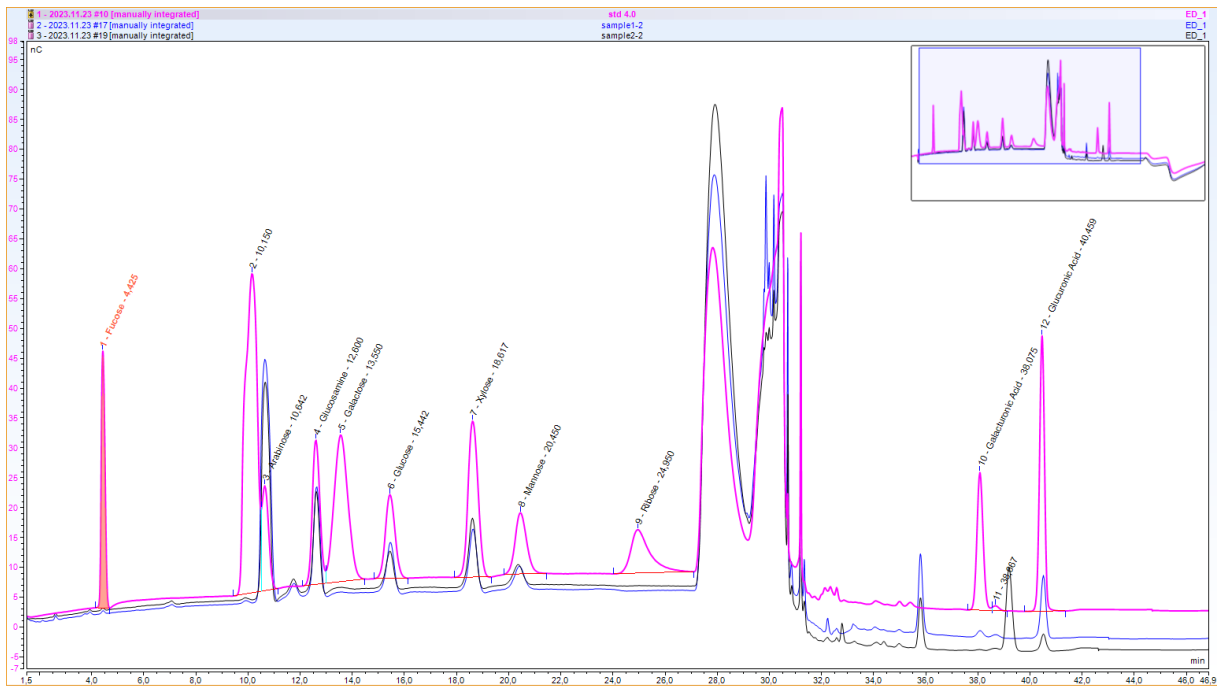
722 **Supplementary Figure S1: FTIR spectrum of 3-50 kDa and >50 kDa AOM fractions.**



723

724

725 **Supplementary Figure S2: HPAEC-PAD chromatogram of sugar standards (pink) and >50 kDa AOM**
726 **samples (blue and dark).**



727

728

729 **Supplementary Table S1:** Jar test set 2- Optimum dosage (minimum dosage corresponding to
 730 maximum SE%), pH, and sigmoidal regression parameters (x_0 , dx) from dose-response curves of
 731 resuspension jar test with AOM permeate fractions (for each sigmoidal regression, $R^2 = 1.00$).

FeCl₃					
Treatments (TOC mg·L ⁻¹)	Optimum Dosage (mg/g dry biomass)	pH	x_0 (mg/g dry biomass)	SE (%)	dx
AOM+ (25.9±2.4)	342.10	3.41	156.4±10.13	99±4	28.02±7.99
AOM- (5.6±1.3)	136.84	3.43	91.74±5.14	98±2	12.95±5.72
<50 kDa (4.6±0.9)	139.37	3.86	67.11±0.94	98±0	1.39±0.00
<3 kDa (4.5±1.5)	139.37	3.89	67.83±0.82	98±1	1.10±0.00

732

NaOH					
Treatments (TOC mg·L ⁻¹)	Optimum Dosage (mg/g dry biomass)	pH	x_0 (mg/g dry biomass)	SE (%)	dx
AOM+ (25.9±2.4)	729.81	10.44	441.7±10.9	100±1	97.78±9.40
AOM- (5.6±1.3)	228.07	10.39	128.52±2.85	100±1	20.01±2.21
<50 kDa (4.6±0.9)	209.06	10.43	151.2±2.82	99±1	6.26±1.28
<3 kDa (4.5±1.5)	209.06	10.43	158.54±0.54	99 ±0	11.19±0.30

733

Chitosan					
Treatments (TOC mg·L ⁻¹)	Optimum Dosage (mg/g dry biomass)	pH	x_0 (mg/g dry biomass)	SE (%)	dx
AOM+ (25.9±2.4)	136.84	7.06	106.07±0.98	99±1	0.93±0.00

AOM- (5.6±1.3)	91.23	6.97	60.27±2.96	97±1	3.09±1.05
<50 kDa (4.6±0.9)	69.69	7.23	55.46±2.2	97±1	0.71±0.00
<3 kDa (4.5±1.5)	69.69	7.27	54.89±1.56	97±1	0.59±0.00

734

735